

## **Locating tectonic tremors with uncertainty estimates: Time- and amplitude-difference optimization, wave propagation-based quality control, and Bayesian inversion**

Takeshi Akuhara<sup>1</sup>, Yusuke Yamashita<sup>2</sup>, Hiroko Sugioka<sup>3</sup>, Masanao Shinohara<sup>1</sup>

<sup>1</sup>Earthquake Research Institute, The University of Tokyo

<sup>2</sup>Disaster Prevision Research Institute, Kyoto University

<sup>3</sup>Department of Planetology, Graduate School of Science, Kobe University

### **Summary**

The accurate location of tectonic tremors helps improve understanding of their underlying physical processes. However, current location methods often do not statistically evaluate uncertainties to a satisfactory degree and do not account for potential biases due to subsurface structures not included in the model. To address these issues, we propose a novel three-step process for locating tectonic tremors. First, the measured time- and amplitude differences between station pairs are optimized to obtain station-specific relative time and amplitude measurements with uncertainty estimates. Second, the time- and amplitude-distance relationships in the optimized data are used to roughly estimate the propagation speed (i.e., shear wave velocity) and attenuation strength. Linear regression is applied to each event, and the resulting velocity and attenuation strength are used for quality control. Finally, the tremor location problem is formulated within a Bayesian framework where the model parameters include the source locations, local site delay/amplification factors, shear wave velocity, and attenuation strength. The Markov chain Monte Carlo algorithm is used to sample the posterior probability and is augmented by a parallel tempering scheme for an efficient global search. We tested the proposed method on ocean-bottom data indicating an intense episode of tectonic tremors in Kumano-nada within the Nankai Trough subduction zone. The results show that typical location errors ( $1\sigma$ ) are  $\sim 1-2$  km horizontally and  $< 5$  km vertically. A series of experiments with different inversion settings reveals that adopting amplitude data and site correction factors help reduce random error and systematic bias, respectively. Probabilistic sampling allows us to spatially map the probability of a tremor occurring at a given location. The probability map is used to identify lineaments of tremor sources, which provides insights into structural factors that favor tremor activity.

## **Key words**

Computational seismology, Body waves, Inverse theory, Subduction zone processes, Seismicity and tectonics

## **1. Introduction**

Tectonic tremors, considered as a swarm of low-frequency earthquakes, constitute a broad spectrum of slow earthquakes together with very low-frequency earthquakes and slow-slip events. They were first discovered in southwestern Japan (Obara, 2002) and have since been identified at subducting plate interfaces worldwide (Araki et al., 2017; Brown et al., 2005; Nishikawa et al., 2019; Payero et al., 2008; Plata-Martinez et al., 2021; Rogers, 2003; Todd et al., 2018; Yamashita et al., 2015). Slow earthquakes, including tectonic tremors, release seismic energy over a long time considering their magnitudes, which indicates that they may be governed by different physical processes than regular earthquakes (Ide et al., 2007). Owing to their proximity to the rupture areas of megathrust earthquakes, slow earthquakes have drawn significant attention for their potential to deepen our understanding of future devastating earthquakes (Obara & Kato, 2016).

The accurate location of tectonic tremors is vital to understanding the slip behavior of plate interfaces. The spatiotemporal evolution of tectonic tremors has several unique but ubiquitous characteristics. First, tremors occur episodically, with their epicenters migrating parallel to the subduction margin, which indicates the simultaneous occurrence of slow-slip events. Second, tremors occasionally back-propagate against their main front at distinctly high speeds, known as rapid tremor reversal (e.g., Houston et al., 2011). Third, streaks of tremors in the dip direction of the subducting plate have been observed (e.g., Ghosh et al., 2010). These spatiotemporal patterns of tremors can constrain the frictional properties of the plate interface (Rubin, 2011), underlying physical processes (Cruz-Atienza et al., 2018), and structural factors that cause tremors (Ide, 2010).

The signals of tectonic tremors emerge without a clear phase onset, which makes locating them using the same methods as for regular earthquakes impractical. A common approach is the envelope correlation method (e.g., Mizuno & Ide, 2019; Obara, 2002), which cross-correlates enveloped seismograms between pairs of stations and assumes that the resulting time lag represents a difference in S-wave travel time. Optimization methods can then be applied to determine the source locations that best explain the measured arrival time differences. Another approach is to use the amplitude (e.g., Husker et al., 2012; Ogiso & Tamaribuchi, 2022), although such techniques are more widely used for locating volcanic tremors rather than tectonic tremors. Because seismic waves lose energy

during propagation, the spatial pattern of amplitudes can provide clues about source locations. However, this approach requires knowledge of attenuation structures and local site amplification, which typically necessitates additional analysis. Some studies have used a joint approach that combines both time- and amplitude-based methods, where the different datasets are often weighted subjectively (Maeda & Obara, 2009).

Despite the importance of investigating the source locations of tectonic tremors, many studies have not formally estimated the uncertainties associated with these locations, which raises the risk of misinterpreting results. Accurately estimating the uncertainties of tremor locations requires considering the statistics of the input measurements in the data domain (i.e., time and amplitude domains) and then converting them into the spatial domain by forward calculation. Uncertainties in the structure model used for the forward calculation must also be considered to prevent systematic biases. Such uncertainties in structures would be severe for offshore studies targeting shallow tectonic tremors (e.g., Yamashita et al., 2015). Typically, the seafloor is covered with unconsolidated sediments. Such near-surface structures amplify the amplitude and delay the arrival of seismic waves, and the degree of this effect varies according to the geographic location.

To address the above issues, we propose a three-step method for locating tectonic tremors and estimating their uncertainty, which we applied to real tremor data obtained at Kumano-nada in the Nankai Trough subduction zone as a demonstration.

## **2. Data**

We collected data from a seismic network at Kumano-nada in the Nankai Trough subduction zone, where the Philippine Sea plate subducts beneath the fore-arc margin. As shown in Fig. 1, the network comprises 16 permanent cabled stations from the Dense Ocean Network for Earthquake and Tsunamis (DONET) (Kaneda et al., 2015; Kawaguchi et al., 2015) and 15 ocean-bottom seismometers (OBSs) temporarily installed from September 2019 to June 2021. All OBSs were equipped with three-component short-period velocity sensors with a natural frequency of 1 Hz. The network includes two micro subarrays (SHM6 and SHM7) each comprising five OBSs, which help with precisely locating tectonic tremors by beam-forming techniques. However, this is beyond the scope of this study.

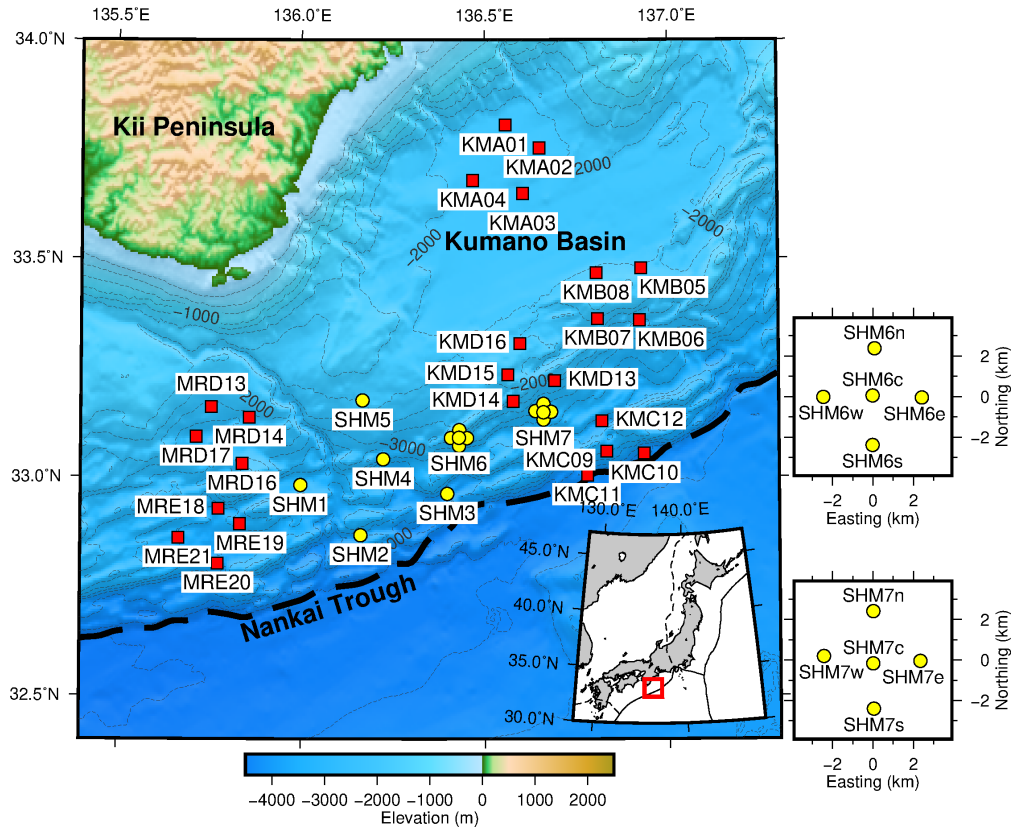


**Figure 1.** Tectonic setting and station arrangement of the study area. The red squares are permanent DONET stations, and the yellow circles are temporary ocean-bottom seismometers (OBSs), which include two micro subarrays (SHM6 and SHM7) each comprising five OBSs with a separation distance of  $\sim 2.5$  km (right panels). The inset shows the configuration of tectonic plates around Japan, where the red square encloses the study area.

Intense episodes of slow earthquakes, including tectonic tremors and very low-frequency earthquakes, repeatedly occur in this region at intervals of  $\sim 5$  years (e.g., Takemura et al., 2022). The latest and most intensive episode began on December 6, 2020, and persisted for approximately 2 months (Ogiso & Tamaribuchi, 2022) within the observation period of the OBSs. We collected data from a 20-day period in the middle of this episode from January 1 to January 21, 2021, during which tremors are known to have occurred near the center of the seismic network (Ogiso & Tamaribuchi, 2022).

Note that our study focuses on accurately locating tectonic tremors rather than attempting to locate them exhaustively. This is why we only used 20 days of data, rather than the  $\sim 2$  months of data covering the entire tremor episode, to reduce computation time. For the same reason, we only briefly describe the tremor detection process below.

To detect the tectonic tremors, we preprocessed continuous seismic waveform data as follows. First, 300-s time windows were successively extracted from the continuous data with 50% overlap. The extracted time series were de-trended, tapered, bandpass-filtered from 1–10 Hz, and converted to envelopes via the Hilbert transform. We then smoothed the resulting envelopes with a 6-s triangular filter and merged the two horizontal components by using the root sum squared method. We did not use the vertical component because shear waves dominate the seismic records of tectonic tremors.

We detected tremors by inter-station cross-correlation. We used the 300-s envelopes to calculate cross-correlation functions between all possible station pairs every 150 s. For each station pair, all obtained correlation values with lag times from -150 s to 150 s were saved over the whole 20-day period to generate a histogram specific to the station pair. We defined tremor detection as when a correlation value exceeded the 98th percentile of the histogram for at least 300 station pairs. Of the 11,520 time windows, 4324 time windows met these criteria.

### **3. Method**

Our proposed method has three steps. Step 1 is to optimize measurements from station pairs such as the arrival time difference and logarithmic amplitude ratio, which outputs the relative arrival time and logarithmic amplitude ratio at each station along with their respective uncertainties. These uncertainties can be incorporated in the final inversion stage to acquire uncertainties in the spatial domain. Step 2 is to extract the first-order features of wave propagation from the optimized station-specific data: the propagation speed and attenuation strength. These features are then used as quality control factors to retain good-quality data. Step 3 is to invert the station-specific data and their uncertainties for hypocenters by using the Markov chain Monte Carlo (MCMC) algorithm in a Bayesian framework. To address biases from unknown structures, we jointly solve multiple hypocenters and include structural parameters and the associated correction factors in the model parameters.

#### **3.1. Step1: Optimization of arrival time and amplitude differences**

The unclear phase onset makes direct measurements of the arrival times of tectonic tremors a challenge. A widely used alternative approach is to use cross-correlation to measure the arrival time difference between station pairs (e.g., Obara, 2002):

$$\Delta t_{ij} \approx \arg \max_{t'} \sum_t u_i(t + t') u_j(t), \quad (1)$$

where  $u_i(t)$  is an envelope waveform recorded at the  $i$ th station and  $\Delta t_{ij}$  is the arrival

time difference between the  $i$ th and  $j$ th stations. This approach only works when the two waveforms are sufficiently similar. If the waveforms differ (e.g., due to different propagation paths), the measured arrival time difference can deviate from the true value. In addition, a high level of noise can easily pose artificial peaks in the cross-correlation functions. Once the arrival time difference is obtained, the amplitude ratio between the two envelopes is defined as follows:

$$\Delta a'_{ij} = \frac{\sum_t u_i(t + \Delta t_{ij})u_j(t)}{\sum_t u_j(t)u_j(t)}. \quad (2)$$

This definition corresponds to the maximum likelihood estimation (MLE) of the amplitude ratio between two similar waveforms (Appendix A). The numerator has already been calculated to find the maximum of the cross-correlation function in Equation (1), so it does not require additional computation. Other definitions than Equation (2) may be used for the amplitude ratio, such as the squared sum (Maeda & Obara, 2009) or median value (Li et al., 2022). The obtained amplitude ratios are converted to amplitude differences by taking the logarithm so that they can be treated mathematically in the same manner as the arrival time differences:

$$\Delta a_{ij} \equiv \ln(\Delta a'_{ij}) = \ln \frac{\sum_t u_i(t + \Delta t_{ij})u_j(t)}{\sum_t u_j(t)u_j(t)}. \quad (3)$$

The above process yields  $N_{sta}(N_{sta} - 1)/2$  pairs of measurements, where  $N_{sta}$  is the number of stations. Individual pair measurements are dependent on other pairs (i.e.,  $\Delta t_{ij} \sim \Delta t_{ik} - \Delta t_{kj}$ ). In other words, the  $N_{sta}(N_{sta} - 1)/2$  measurements inherently include redundancy. We may optimize this redundancy by solving a linear system (VanDecar and Crosson, 1990):

$$\begin{pmatrix} 1 & -1 & 0 & 0 & \cdots & 0 & 0 & 0 & 0 \\ 1 & 0 & -1 & 0 & \cdots & 0 & 0 & 0 & 0 \\ & & & \vdots & & & & & \\ 0 & 0 & 0 & 0 & \cdots & 0 & 1 & 0 & -1 \\ 0 & 0 & 0 & 0 & \cdots & 0 & 0 & 1 & -1 \\ 1 & 1 & 1 & 1 & \cdots & 1 & 1 & 1 & 1 \end{pmatrix} \begin{pmatrix} t_1^{rel} \\ t_2^{rel} \\ \vdots \\ t_{N_{sta}-1}^{rel} \\ t_{N_{sta}}^{rel} \end{pmatrix} = \begin{pmatrix} \Delta t_{12} \\ \Delta t_{13} \\ \vdots \\ \Delta t_{N_{sta}-2, N_{sta}} \\ \Delta t_{N_{sta}-1, N_{sta}} \\ 0 \end{pmatrix}, \quad (4)$$

where  $t_1^{rel} \dots t_{N_{sta}}^{rel}$  denote the relative arrival time at each station. A regularization condition is added to the bottom row that imposes a zero-sum requirement on the relative arrival times. This system has the following analytical solution (VanDecar & Crosson, 1990):

$$t_i^{rel} = \frac{1}{N_{sta}} \sum_{i \neq j} \Delta t_{ij}. \quad (5)$$

This optimization reduces the redundant measurements of  $N_{sta}(N_{sta} - 1)/2$  station pairs to  $N_{sta}$  individual station-specific measurements. The original redundancy reflects

the measurement errors. The corresponding standard deviation can be calculated as follows (VanDecar & Crosson, 1990):

$$\sigma_i^{time} = \sqrt{\frac{\sum_{i \neq j} [\Delta t_{ij} - (t_i^{rel} - t_j^{rel})]^2}{N_{sta} - 2}}. \quad (6)$$

The later Bayesian inversion in Step 3 takes the above station-specific relative arrival times ( $t_i^{rel}$ ) as input data, and their standard deviation ( $\sigma_i^{time}$ ) are used for calculating the likelihood.

Similar equations hold for logarithmic amplitudes:

$$a_i^{rel} = \frac{1}{N_{sta}} \sum_{i \neq j} \Delta a_{ij}, \quad (7)$$

and

$$\sigma_i^{amp} = \sqrt{\frac{\sum_{i \neq j} [\Delta a_{ij} - (a_i^{rel} - a_j^{rel})]^2}{N_{sta} - 2}}, \quad (8)$$

where  $a_i^{rel}$  is a relative logarithmic amplitude at the  $i$ th station, and  $\sigma_i^{amp}$  is the corresponding standard deviation.

Fig. 2 demonstrates the effectiveness of the proposed method when applied to an example event. The envelopes exhibit improved coherency after being shifted in time by the optimized values (Fig. 2a) and scaled in amplitude (Fig. 2b). We found that the proposed optimization works well with good-quality data that shows high signal-to-noise ratios across the entire network. Typical failures involve an insufficient signal level at some stations, which results in poor temporal alignments by cross-correlation (Fig. S1). Such poor-quality data, even if present at only a few stations, can distort the optimized solution significantly because the optimized solutions given by the arithmetic mean (i.e., Equations (5) and (7)) are not robust against outliers. This sensitivity to poor-quality data requires an automatic and objective process to reject ill-optimized results.



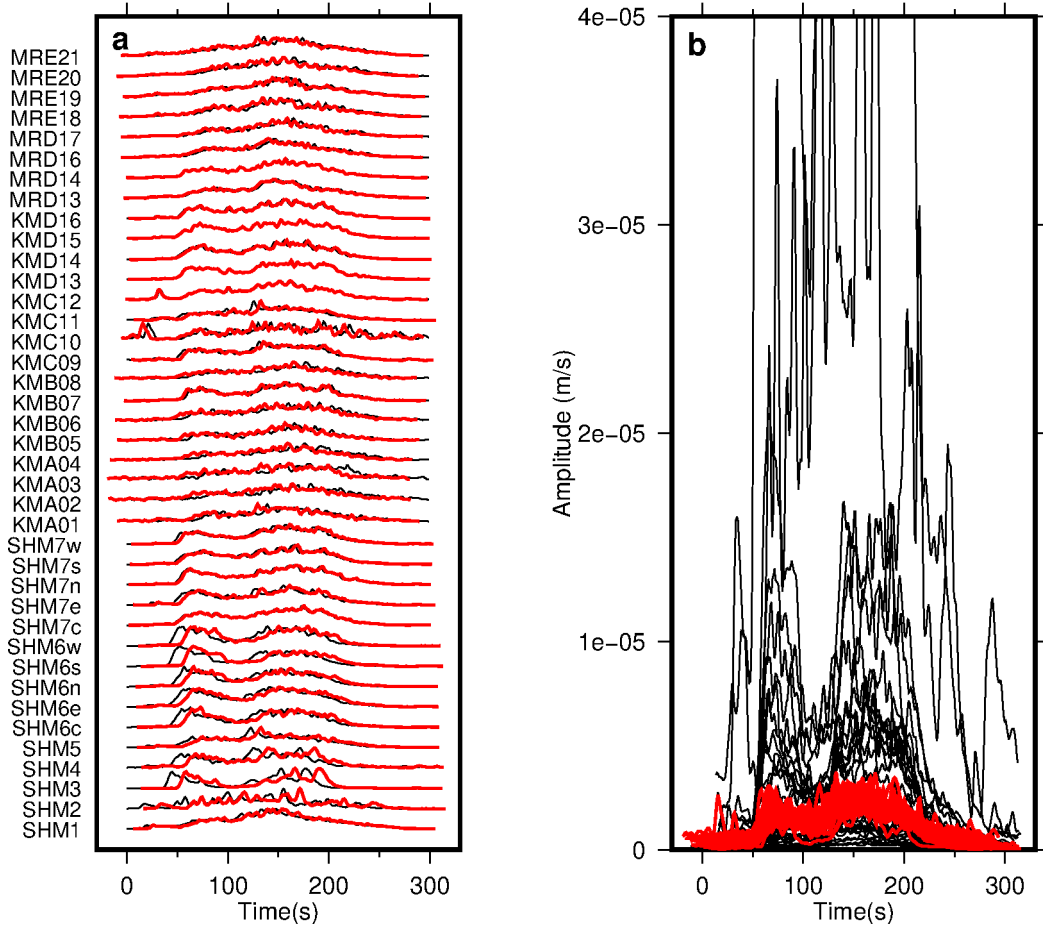


Figure 2. Tremor envelopes before optimization (black) and after optimization (red) of a specific event: (a) time-difference data and (b) amplitude-difference data. In (a), the station names are listed along the vertical axis.

### 3.2. Step2: Wave propagation-based quality control

The optimization in Step 1 is useful for capturing seismic wave propagation intuitively. In cases where the optimization is successful and not affected by outliers, the relative arrival times and amplitudes exhibit a concentrated pattern when viewed on a map where the center approximates the epicenter, as shown in Fig. 3. We can use this pattern to obtain time–distance and amplitude–distance relationships, which in turn can be used to roughly quantify the propagation speed (i.e., S-wave velocity  $V_S$ ) or attenuation strength (i.e., quality factor  $Q_S$ ), respectively.

For a uniform velocity structure throughout the medium, the arrival time  $t^{syn}$  is proportional to the propagation distance  $d$ :

$$t^{syn} = \frac{d}{V_S}. \quad (9)$$



Thus,  $V_S$  can be estimated from the slope of the time–distance plot (Fig. 3c).

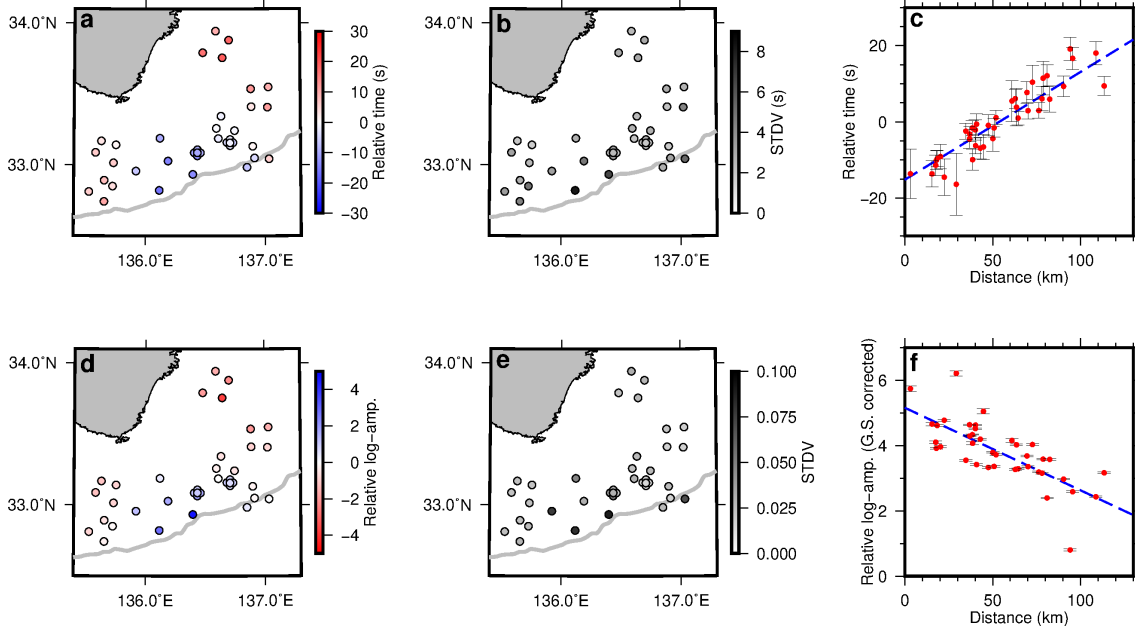


**Figure 3.** (a–c) Time and (d–f) amplitude optimizations of a specific event. (a, d) The optimized station-specific measurements are shown in map view. The gray line denotes the trench. (b, e) Corresponding standard deviations obtained from Equations (6) and (8). (c, f) Distance plots of the optimized station-specific measurements. The error bar denotes the standard deviation. The blue dashed line represents a regression line.

The amplitude of a body wave at a propagation distance  $d$  is described as

$$a'^{syn} = a_0 \frac{\exp(-Bd)}{d}, \quad (10)$$

$$B = \frac{\pi f}{Q_S V_S}, \quad (11)$$

where  $a_0$  is the source amplitude,  $f$  is the representative frequency, and  $Q_S$  is the quality factor. Taking the logarithm of Equation (10) leads to

$$a^{syn} \equiv \ln(a'^{syn}) = -Bd + \ln a_0 - \ln d. \quad (12)$$

After correcting the geometrical spreading (i.e., adding  $\ln d$  to Equation (12)), the logarithmic amplitude becomes proportional to the distance. Therefore, we can determine the attenuation strength  $B$  from the slope of the amplitude–distance plot (Fig. 3f).

We propose using the estimated  $V_S$  and  $B$  (or  $Q_S$  if  $f$  and  $V_S$  are fixed) as quality control factors to select good-quality events. The estimated  $V_S$  and  $B$  are representative of a broad region where source–receiver paths pass through. Because

tectonic tremors always occur in a narrow depth range, all ray paths most likely propagate through similar depths. Considering that subsurface properties vary less laterally than vertically, the estimated  $V_S$  and  $B$  values from different events should fall into a narrow and physically reasonable range. Hence, events with outlier  $V_S$  and  $B$  values can be attributed to ill-optimized datasets or events far isolated from target tremors, such as teleseismic events.

In practice, the propagation distance  $d$  is not known before the hypocenter is determined. Instead, we may assume that the source is located beneath the station with the maximum relative amplitude. In this study, we assume that the focal depth is 7 km below sea level considering the specific tectonics of the study area. The resulting distance plots from the assumed source location are then linearly regressed by the least squares method. The resultant  $V_S$  and  $B$  values from different events are shown in Fig. 4. Based on the scatter plot, we selected events with  $V_S=2.0\text{--}4.0$  km/s and  $B=0.015\text{--}0.030$  as acceptable. These ranges are comparable to those previously estimated for the study area (Akuhara et al., 2020; Yabe et al., 2021), and they correspond to  $Q_S$  of 130–520 if a dominant frequency of 5 Hz is assumed. Under this criteria, 580 of the 4324 events were retained.

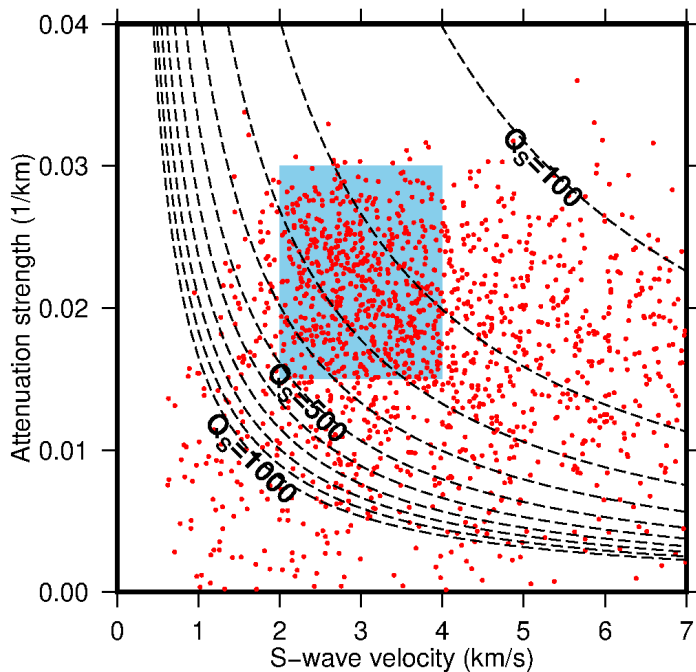


Figure 4. Estimations of the S-wave velocity ( $V_S$ ) and attenuation strength ( $B$ ) based on the wave propagation pattern. Each red dot shows the results from different events. The dashed curves are contours of the quality factor ( $Q_S$ ) from 100 to 1000. A dominant frequency of 5 Hz was assumed. The acceptable ranges of  $V_S$  and  $B$  are highlighted in

sky blue.

The above wave propagation-based criteria offer several advantages over conventional non-physics-based quality control factors, such as those based on cross-correlations. In our approach, thresholding values can be selected based on existing knowledge of rock properties ( $V_S$  and  $Q_S$ ) in the study area. In contrast, cross-correlation values have no clear physical interpretation, and their values highly depend on analysis conditions such as frequency ranges and time window lengths. Local site conditions also influence correlation values. In addition, our proposed criteria ensure that the global minimum exists near the propagation center during the hypocenter determination. In contrast, thresholding by cross-correlation cannot guarantee a global minimum even if cross-correlation values are high. This can be illustrated by teleseismic events, where waveforms exhibit high coherency among stations but no global minimum can be identified.

### **3.3. Step 3: Bayesian inversion**

In Step 3, we adopt a Bayesian interface to invert the relative arrival times and logarithmic amplitudes jointly for the hypocenters ( $x_j, y_j, z_j; j = 1, \dots, N_{evt}$ ), delay factor for each station ( $\tau_i^{sta}; i = 1, \dots, N_{sta}$ ), amplification factor for each station ( $\alpha_i^{sta}; i = 1, \dots, N_{sta}$ ), S-wave velocity ( $V_S$ ), and quality factor ( $Q_S$ ). Here,  $N_{sta}$  and  $N_{evt}$  represent the numbers of stations and events, respectively. The delay and amplification factors are used to account for the local effects caused by seafloor sediment beneath the stations. We assumed uniform structures for the S-wave velocity and attenuation for simplicity. These model parameters are denoted by  $\mathbf{m}$  hereafter.

The optimized station-specific measurements and their uncertainties given by Equations (5)–(8) are used as inputs for the inversion. To distinguish different events, we append a subscript to the notation of these inputs. For instance,  $t_{ij}^{rel}$  has the same meaning as  $t_i^{rel}$  in Equation (5) but is for the  $j$ th event.  $a_{ij}^{rel}$ ,  $\sigma_{ij}^{time}$ , and  $\sigma_{ij}^{amp}$  are defined in a similar manner. Furthermore, the following vector notation is used:

$$\mathbf{d}^{time} = (t_{11}^{rel} \dots t_{ij}^{rel} \dots t_{N_{sta}N_{evt}}^{rel})^\top, \quad (13)$$

$$\mathbf{d}^{amp} = (a_{11}^{rel} \dots a_{ij}^{rel} \dots a_{N_{sta}N_{evt}}^{rel})^\top, \quad (14)$$

$$\boldsymbol{\sigma}^{time} = (\sigma_{11}^{time} \dots \sigma_{ij}^{time} \dots \sigma_{N_{sta}N_{evt}}^{time})^\top, \quad (15)$$

$$\boldsymbol{\sigma}^{amp} = (\sigma_{11}^{amp} \dots \sigma_{ij}^{amp} \dots \sigma_{NstaNevt}^{amp})^\top. \quad (16)$$

The posterior probability of the model parameters ( $\mathbf{m}$ ) can be written as  $P(\mathbf{m}|\mathbf{d}^{time}, \mathbf{d}^{amp}) = CP(\mathbf{m})\mathcal{L}^{time}(\mathbf{d}^{time}, \boldsymbol{\sigma}^{time})\mathcal{L}^{amp}(\mathbf{d}^{amp}, \boldsymbol{\sigma}^{amp})$ , (17) where  $P(\mathbf{m})$  is the prior probability;  $\mathcal{L}^{time}(\mathbf{d}^{time}, \boldsymbol{\sigma}^{time})$  and  $\mathcal{L}^{amp}(\mathbf{d}^{amp}, \boldsymbol{\sigma}^{amp})$  are the likelihoods of the time and amplitude data, respectively; and  $C$  is a normalization constant. Direct computation of Equation (17) is infeasible because the normalization constant involves integration over the entire model space. However, the posterior probability can be estimated via probabilistic sampling, such as with the MCMC algorithm.

We assumed a Gaussian distribution for the prior probability of the horizontal locations, station correction terms, S-wave velocity, and attenuation factor:

$$P(\theta) = \frac{1}{\sqrt{2\pi\sigma_{prior}^\theta}^2} \exp\left[-\frac{(\theta - \mu_{prior}^\theta)^2}{2\sigma_{prior}^\theta{}^2}\right], \quad (18)$$

where  $\mu_{prior}^\theta$  and  $\sigma_{prior}^\theta$  are the mean and standard deviation, respectively, and  $\theta$  is either  $x_j$ ,  $y_j$ ,  $\tau_i^{sta}$ ,  $\alpha_i^{sta}$ ,  $V_S$ , or  $Q_S$ . We adopted Rayleigh distribution for event depths:

$$P(z_j) = \frac{z_j - z_0}{\sigma_{prior}^{z_j}} \exp\left(-\frac{(z_j - z_0)^2}{2\sigma_{prior}^{z_j}{}^2}\right). \quad (19)$$

Here,  $z_0$  is added to the usual formulation of the Rayleigh distribution. Without this term, the Rayleigh distribution is defined for positive values (i.e.,  $z > 0$ ). Adding  $z_0$  changes the domain to  $z > z_0$ . Introducing  $z_0$  may be useful for prohibiting hypocenters located above the seafloor, although we found that it did not affect the results significantly.

Table 1 presents the selected parameter values for these priors. Note that the selected parameter values have a minimal impact on the posterior probability except in cases where extremely narrow ranges are employed. This insensitivity aligns with theoretical expectations: as the amount of data increases, the weight of the prior probability on the posterior probability exponentially decays. This behavior should not be confused with the regularization often used in geophysical inversion, which suppresses solutions that deviate from the initial model. In such analyses, the regularization weight is determined ad hoc regardless of the amount of data.

Table 1. Parameter selection for the prior probability

Description	Notation	Values used
-------------	----------	-------------

Event horizontal locations (Equation (18))	$\mu_{prior}^{x_j}, \mu_{prior}^{y_j}$	Station location showing the maximum amplitude
	$\sigma_{prior}^{x_j}, \sigma_{prior}^{y_j}$	30 km
Event depth (Equation (19))	$\sigma_{prior}^{z_j}$	10 km
	$z_0$	0 km
Delay factor (Equation (18))	$\mu_{prior}^{\tau_i}$	0 s
	$\sigma_{prior}^{\tau_i}$	0.5 s
Amplification factor (Equation (18))	$\mu_{prior}^{\alpha_i}$	0 (= 0 dB)
	$\sigma_{prior}^{\alpha_i}$	0.02 (= 0.09 dB)
S-wave velocity (Equation (18))	$\mu_{prior}^{V_S}$	3.0 km/s
	$\sigma_{prior}^{V_S}$	1.0 km/s
Quality factor (Equation (18))	$\mu_{prior}^{Q_S}$	250
	$\sigma_{prior}^{Q_S}$	100

The likelihood function for the arrival time can be defined as follows:

$$\mathcal{L}^{time}(\mathbf{d}^{time}, \boldsymbol{\sigma}^{time}) = \prod_{i=1}^{N_{sta}} \prod_{j=1}^{N_{evt}} \frac{1}{\sqrt{2\pi\sigma_{ij}^{time^2}}} \exp \left\{ -\frac{[t_{ij}^{syn}(x_i, y_i, z_i, V_S) + \tau_i^{sta} - t_{ij}^{rel} - \tau_j^{evt}]^2}{2\sigma_{ij}^{time^2}} \right\}, \quad (20)$$

where  $t_{ij}^{syn}$  is the predicted arrival time based on the hypocenter and S-wave velocity, and the subscripts  $i$  and  $j$  correspond to station and event indices, respectively. Because only the relative arrival times are known, Equation (20) includes an unknown event-specific time shift term  $\tau_j^{evt}$ . Rather than solving for this term, we set it to the MLE:

$$\tau_j^{evt} = \frac{\sum_{i=1}^{N_{sta}} \frac{t_{ij}^{syn}(x_i, y_i, z_i, V_S) + \tau_i^{sta} - t_{ij}^{rel}}{\sigma_{ij}^{time^2}}}{\sum_{i=1}^{N_{sta}} \frac{1}{\sigma_{ij}^{time^2}}}. \quad (21)$$

Note that Equation (21) corresponds to the averaged residual over stations weighted by

data variance. Similar equations hold for the logarithmic amplitudes:

$$\mathcal{L}^{amp}(\mathbf{d}^{amp}, \boldsymbol{\sigma}^{amp}) = \prod_{i=1}^{N_{sta}} \prod_{j=1}^{N_{evt}} \frac{1}{\sqrt{2\pi\sigma_{ij}^{amp2}}} \exp \left\{ -\frac{[a_{ij}^{syn}(x_i, y_i, z_i, V_S, Q_S) + \alpha_i^{sta} - a_{ij}^{rel} - \alpha_j^{evt}]^2}{2\sigma_{ij}^{amp2}} \right\}, \quad (22)$$

$$\alpha_j^{evt} = \frac{\sum_{i=1}^{N_{sta}} \frac{a_{ij}^{syn}(x_i, y_i, z_i, V_S, Q_S) + \alpha_i^{sta} - a_{ij}^{rel}}{\sigma_{ij}^{amp2}}}{\sum_{i=1}^{N_{sta}} \frac{1}{\sigma_{ij}^{amp2}}}. \quad (23)$$

Notably, the term for source amplitude  $a_0$  is canceled out when Equation (12) is substituted into Equations (22) and (23), which eliminates the need to estimate the source amplitude beforehand.

Based on Equations (17)–(23), we can use the MCMC algorithm to sample the posterior probability. At each iteration, one of the model parameters is perturbed randomly, where the amount of perturbation is drawn from a zero-mean Gaussian distribution with a standard deviation, as given in Table 2. This modification is accepted or rejected in accordance with the Metropolis–Hasting criteria. In this study, we performed 4 million iterations, with the first 2 million iterations treated as a burn-in period. The sampled model parameters were saved at every 500 iterations during the second 2 million iterations. We ran 100 chains of the MCMC algorithm in parallel and allowed them to mutually interact by using a parallel tempering technique for an efficient global search (Geyer, 1991; Sambridge, 2014). We set 20 Markov chains with a unit temperature, while the remaining 80 chains were assigned temperatures between 1 and 2000. A chain pair was randomly selected, and their temperatures were swapped at a certain probability to maintain the detailed balance (Sambridge, 2014). We repeated this temperature swap process 10 times per iteration.

Table 2. Random walk parameters for the MCMC algorithm

Parameter to be perturbed	Standard deviation used to retrieve the perturbation amount
$x_j$	2.0 km
$y_j$	2.0 km
$z_j$	0.4 km
$\tau_i^{sta}$	0.03 s
$\alpha_j^{sta}$	0.005 (= 0.022 dB)

$V_S$	0.2 km/s
$Q_S$	5

## 4. Results and discussion

### 4.1. Inversion results

We applied the above inversion method of Step 3 to the amplitude and time data from the 580 events that passed the quality control in Step 2. The likelihood almost monotonically increased with the number of iterations and converged within the burn-in period (Fig. 5a, black dots), which suggests that model parameters sampled after the burn-in period can simulate the posterior probability. To evaluate the effect of the parallel tempering scheme, we conducted a parallel inversion analysis using 100 MCMC chains but without tempering. Although the likelihood increased at a slower pace than the tempered analysis (Fig. 5a, gray dots), most chains reached the same likelihood level as the tempering method at the 250,000th iteration (Fig. 5b). This good performance even without a tempering scheme likely reflects a well-posed inverse problem. As noted earlier, the quality control in Step 2 ensures a well-defined global minimum, which allows the inverse problem to be solved efficiently.

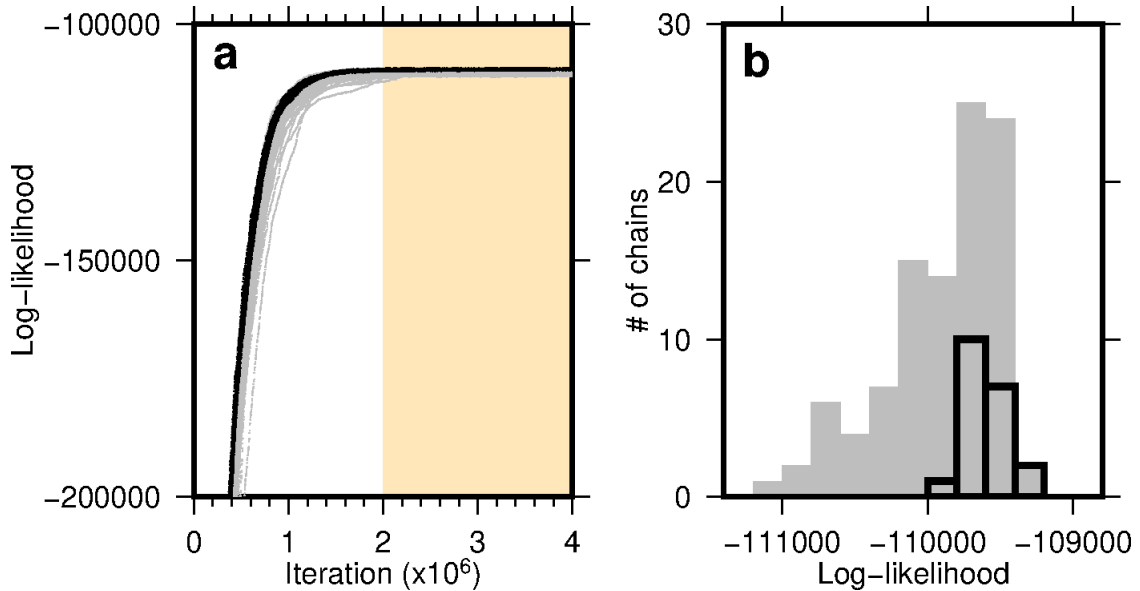


**Figure 5.** (a) Likelihood evolution. Black dots show the likelihood of MCMC samples by 20 non-tempered chains. The underlying gray dots show the results of independent inversion without parallel tempering for which 100 non-tempered chains were employed. The yellow-shaded area highlights iterations after the burn-in period. (b) Histograms of the likelihood sampled by non-tempered MCMC chains at the 250,000th iteration. The



black and gray histograms show the results with and without the tempering scheme, respectively.

The inversion results are summarized in Fig. 6. Note that similar results were obtained from the non-tempered analysis (Fig. S2). The epicenters, which we defined as the mean of the MCMC samples, are tightly clustered in the map view. The typical horizontal location uncertainties ( $1\sigma$ ) derived from the MCMC samples are  $<2$  km in the east–west direction (blue histogram in Fig. 7a) and  $<3$  km in the north–south direction (blue histogram in Fig. 7b). The errors are slightly less in the east–west direction than in the north–south direction because the seismic network geometry is elongated in the east–west direction and variation of the subsurface structures is relatively gentle in the trench–parallel direction. The typical vertical uncertainties are  $<5$  km (blue histogram in Fig. 7c). Unfortunately, the vertical uncertainties are insufficient to discuss the source faults of the tectonic tremors considering the subduction depth of  $\sim 6$ – $8$  km. Because of this loose constraint on the depth, some hypocenters are located above the seafloor. We may explicitly prohibit such unlikely solutions by increasing  $z_0$  in Equation (19), although this change had almost no influence on the horizontal locations (Fig. S3).

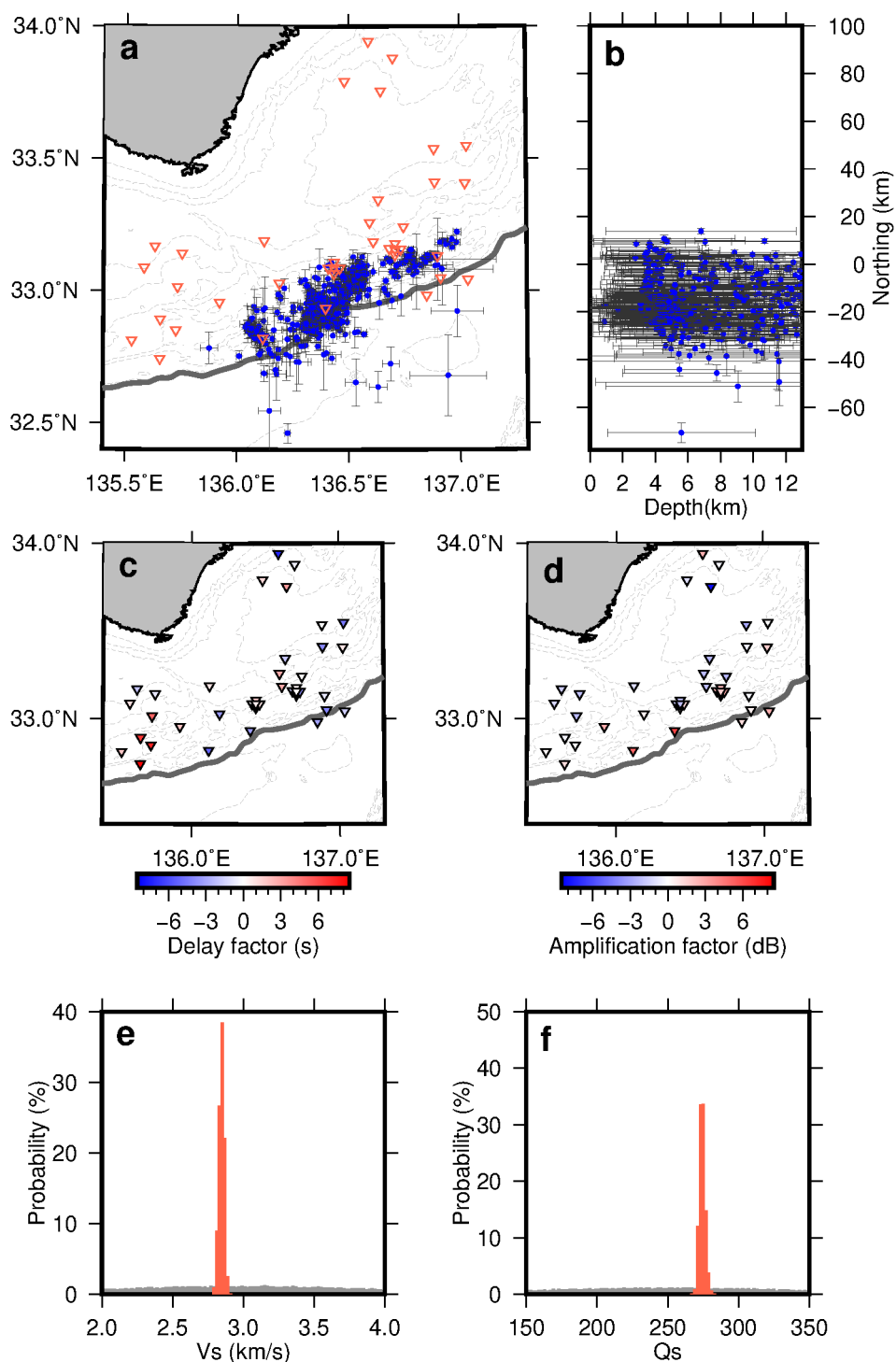
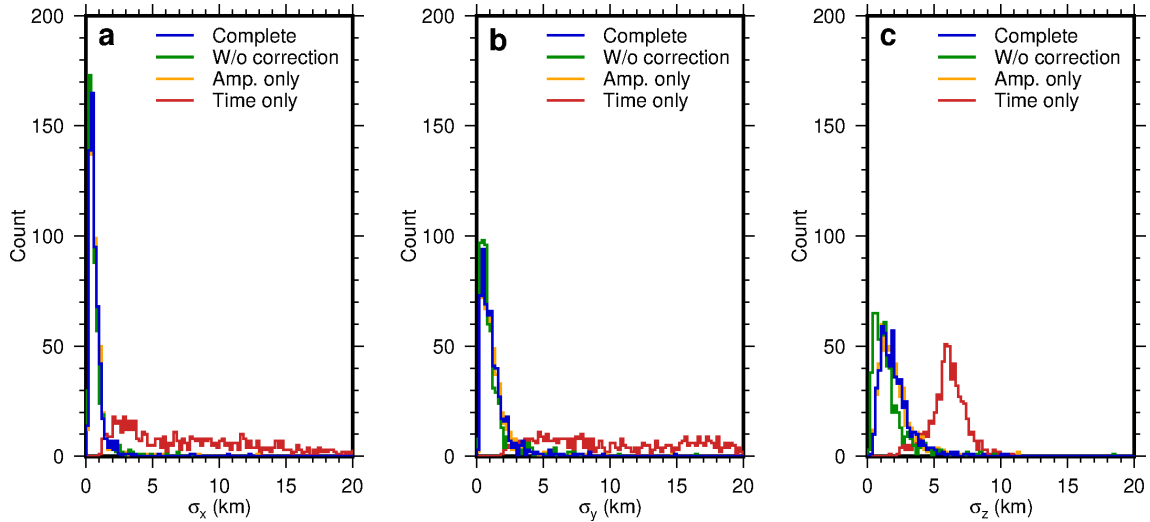


Figure 6. Inversion results. (a, b) Hypocenters. Each blue dot shows the mean hypocenter of the MCMC samples for each event. The error bars represent a  $2\sigma$  uncertainty range assuming a normal distribution for the MCMC samples. The inverted triangles are seismic stations. The thick gray line represents the trench. Mean (c) delay factors and (d) amplification factors of the MCMC samples. Probability distributions of the (e) S-wave

velocity and (f) quality factor. Red and gray histograms show the posterior and prior distributions, respectively.



**Figure 7.** Histograms of the hypocenter uncertainties ( $1\sigma$ ) in the (a) east–west, (b) north–south, and (c) vertical directions. The differently colored histograms show the hypocenter uncertainties from different inversion settings: the complete case (blue), without correction terms (green), amplitude data only (orange), and time data only (red).

The mean values of the correction factors range from  $-7.3$  to  $8.4$  s for time delays and from  $-8.1$  to  $6.2$  dB for amplification (Figs 6c and d). Overall, these values exhibit a smooth lateral variation, with stations near the trench experiencing earlier arrivals and a more significant amplification than predicted. The thinner accretionary prism near the trench likely explains the early arrivals, which allows seismic waves to travel through the subducted crust at faster velocities. In addition, the significant amplification at the trench is reasonable because the trench-fill sediments are less consolidated than the landward accretionary prism (Tsuji et al., 2011). Station MRE20 exceptionally shows a delayed arrival near the trench. Because this station is separated from the majority of events, this delayed arrival may account for the structural heterogeneities in the trench-parallel direction.

The posterior probabilities of the S-wave velocity and quality factor have narrow peaks, with mean values of  $2.85$  km/s and  $274$ , respectively (Figs 6e and f). These values correspond to an attenuation strength of  $2.00 \times 10^{-2}$  km $^{-1}$ , and they are consistent with those obtained from the regression analysis (Fig. 4). The S-wave velocity of  $2.85$  km/s is somewhat slower than that reported for the oceanic crust of this region ( $>3$  km/s) but is comparable to the velocity of the underthrust sediment immediately above the crust

(Akuhara et al., 2020). Yabe et al. (2021) independently estimated the attenuation strength of this region as a function of the hypocentral distance by using the seismic amplitudes of tectonic tremors that occurred in different periods, and their results are mostly consistent with our estimations.

#### **4.2. Contributions of each factor**

The proposed method offers several improvements compared to conventional analyses. For better understanding of its advantages, the contributions of different factors need to be considered, and hence we performed inversion under different settings (**Fig. 8**). **Fig. 8(a)** shows the inversion results from **Fig. 6** (i.e., complete case). **Fig. 8(b)** shows the inversion results when the delay and amplification factors are excluded by setting their values to zero (i.e., without-correction case). **Fig. 8(c)** shows the inversion results when the time difference data are excluded and only the amplitude information was used (i.e., amplitude-only case). In this case, the amplification and quality factors are solved while the S-wave velocity  $V_S$  is fixed at 3.0 km/s. This fixed  $V_S$  value affects the estimation of  $Q_S$  through Equation (11) but not the other parameters. **Fig. 8(d)** shows the inversion results when only the time data are used with the S-wave velocity and delay factors solved (i.e., time-only case). This case does not involve the attenuation parameter.

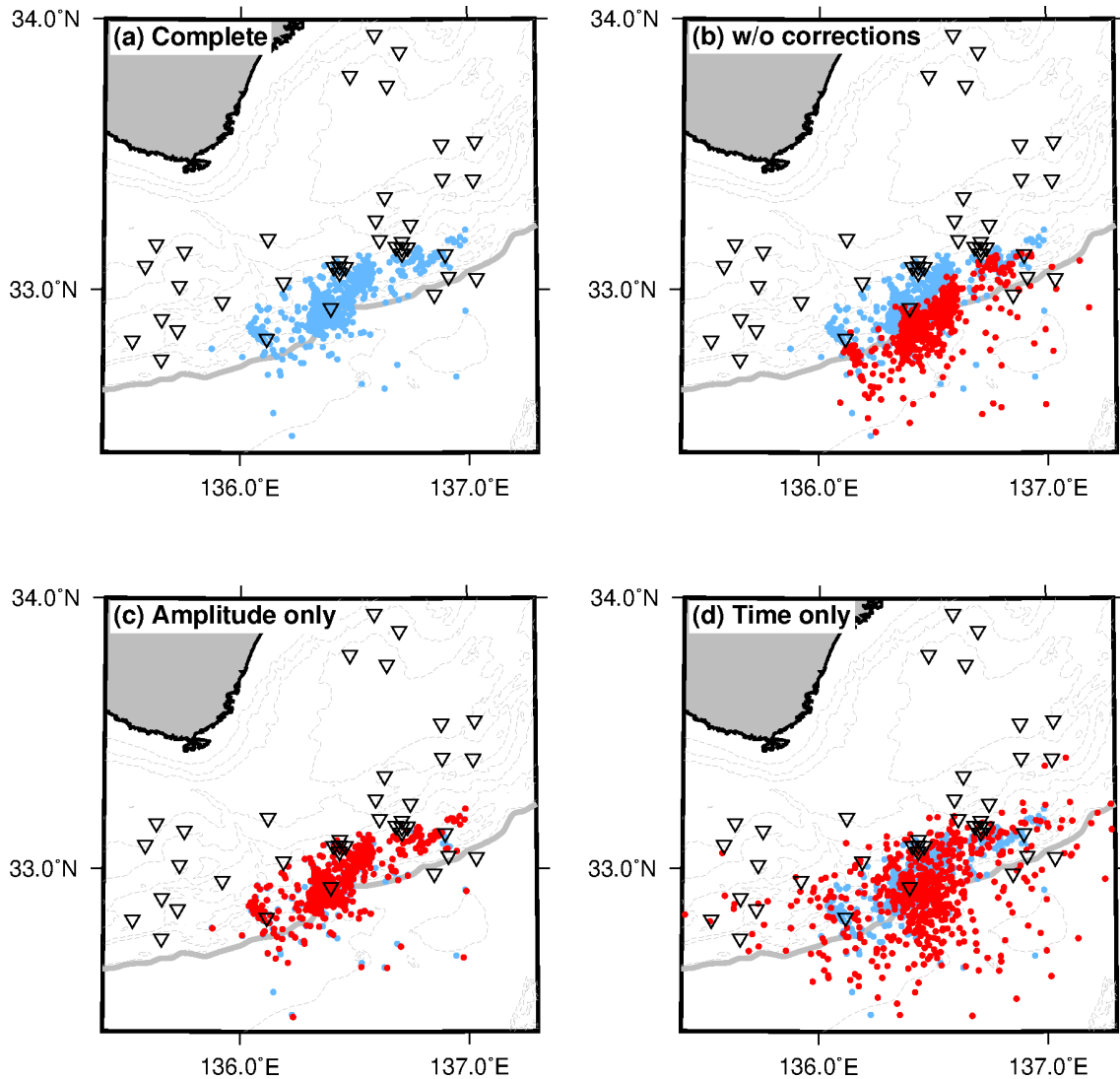


**Figure 8.** Inversion results under different settings: (a) complete, (b) without corrections (i.e., amplification and delay factors), (c) amplitude data only, and (d) time data only. The pale-blue dots are hypocenters (i.e., mean values of the MCMC samples) in the complete case. The red dots are the resultant hypocenters in the other cases. The inverted triangles are seismic stations. The gray line represents the trench.

In the without-correction case, the hypocenters are systemically located further seaward than in the complete case. Although we do not know the true hypocenters, the without-correction case shifts many events seaward of the trench, which is highly unlikely. We conjecture that adding correction factors accounts for structural heterogeneities in the along-dip direction, which helps correct this artificial shift. The seaward shift is  $\sim 10$  km on the western side, where station coverage is relatively limited. These shifts are greater than the uncertainties of the hypocenters shown in Figs 7(a) and (b). Failing to consider

these corrections can significantly bias the results and lead to misinterpretation.

The time-only case suffers from a greater uncertainty for the hypocenters than the amplitude-only case (Fig. 7). The hypocenters are more scattered in space in the time-only case (Fig. 8d) whereas they are similar to the complete case in the amplitude-only case (Fig. 8c). These discrepancies can be attributed to the considerable uncertainty in the time data, which can be quantitatively understood from the distance plots in Figs 3(c) and 3(f). For example, the typical error in time  $\sigma^{time}$  can be read as 5 s from Fig. 3(c) while the typical error in amplitude  $\sigma^{amp}$  can be read as 0.05 from Fig. 3(f). The typical errors in epicenter can then be calculated as  $\sigma^{time} \cdot (\partial T/\partial d)^{-1}$  or  $\sigma^{amp} \cdot (\partial A/\partial d)^{-1}$ , where  $\partial T/\partial d$  and  $\partial A/\partial d$  represent the slopes of the regression lines in the time–distance and amplitude–distance plots, respectively. If  $\partial T/\partial d$  is  $0.3 \text{ s} \cdot \text{km}^{-1}$  and  $\partial A/\partial d$  is 0.03, the error for the epicenter is 17 km using time data and 1.7 km using the amplitude data, which indicates a difference of an order of magnitude.

The large uncertainties in the time data can be attributed to the inconsistencies in the lag-time measurements between station pairs. Takemura et al. (2020) showed that a slow and heterogeneous accretionary prism complicates tremor waveforms as they propagate over longer distances. Lag-time measurements between stations at greater distances from each other are more susceptible to this waveform distortion, which can increase measurement inconsistency. A common strategy to mitigate this issue is to limit station pairs to those with shorter distances or high coherencies. However, such data selection is often based on subjective criteria.

Our results demonstrate the superiority of amplitude data for tectonic tremor location because it can pose tight constraints on hypocenters without any ad hoc selection of data. Challenges associated with using amplitude data may include difficulties with estimating the source amplitude, attenuation structure, and local site effects beforehand. However, the proposed inversion approach eliminates the need for these prerequisite processes.

### **4.3. Spatiotemporal evolution of tremors**

The proposed method provides well-constrained epicenters with typical estimation uncertainties of  $<2 \text{ km}$ . This allows the spatiotemporal evolution of the tremor activity to be discussed in detail. As shown in Fig. 9(a), the located tremors can be divided into three main groups (A–C) separated by gaps of  $\sim 10 \text{ km}$ . Fig. 9(b) shows that, during the first 9 days of the study period, source locations within group A mainly migrate to the east along the trough margin at a speed of  $\sim 2 \text{ km/day}$  (phases i–iii). Such migration of tremors has been commonly observed worldwide, and it is thought to reflect an undergoing slow slip

event. In the middle of this period (i.e., phase ii), group B showed some tremor activity to the west. Although the gap between groups A and B makes it difficult to conclude the migration pattern, the tremor epicenters appear to show a westward migration at a speed of 8 km/s in phases i–ii. Once the main eastward migration reached group C, the migration speed abruptly changed to  $\sim 13$  km/day (phase iv). This fast migration lasted for 3 days. Then, after a quiescence period of about 1 day, relatively small-scale activity occurs in the northeastern part of Group A (phase v; see orange epicenters in Fig. 9a). The observed spatiotemporal evolution of the tremors is roughly consistent with that described by Ogiso & Tamaribuchi (2022), who used amplitude data from DONET stations to determine tremor locations.

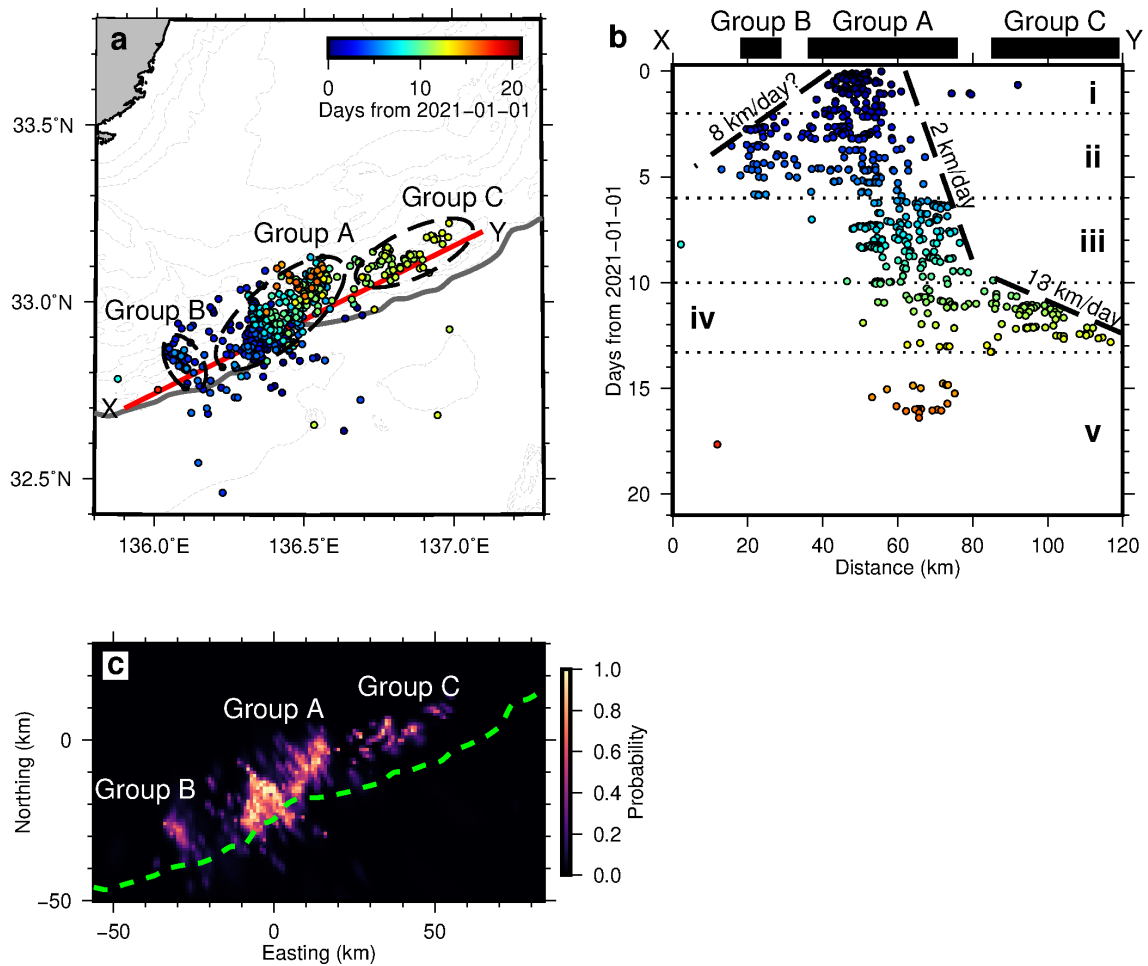


Figure 9. Spatiotemporal evolution of tremors. (a) Map view of tremor epicenters with colors corresponding to days of the study period. The gray line represents the trench. (b) Temporal evolution of tremors projected along the X–Y profile (red line in (a)). The color notation corresponds to that in (a). (c) Probability of at least one tremor epicenter being



located within a  $1 \text{ km} \times 1 \text{ km}$  cell. The green dashed line represents the trench.

Our use of the stochastic sampling technique facilitated the exploration of subtle features within the tremor patterns while minimizing the risk of misinterpretation. For example, we can calculate the probability that any tremor epicenter is located at a particular geographical point  $(x, y)$  as  $p_{any}(x, y) = 1 - \prod_{i=1}^{N_{evt}} [1 - p_i(x, y)]$ , where  $p_i(x, y)$  denotes the marginalized posterior probability for the  $i$ th event epicenter  $(x_i, y_i)$ . Visualizing this probability allows us to identify fine-scale spatial patterns of tremors without being disturbed by events with large uncertainties because such uncertain events have a limited impact on  $p_{any}$ .

Fig. 9(c) shows the obtained map of  $p_{any}$ , which reveals striations of tremors that are difficult to deduce from the standard epicenter map in Fig. 9(a). The epicenters of groups A and B exhibit lineaments oriented toward the direction perpendicular to the trench, while the tremors in group C form trench-parallel lineaments. The trench-normal features observed in groups A and B may originate from the past subduction of rough topography, similar to what has been interpreted for deep tectonic tremors in southwestern Japan (Ide, 2010). The trench-parallel features of group C are likely associated with the topography of the decollement (Hashimoto et al., 2022). This disparity in the distribution patterns may correspond to differences in the migration speed, although a more detailed analysis is outside the scope of this study.

## **5. Conclusions and future perspectives**

We proposed a novel three-step method for locating tectonic tremors that employs the optimization of pair-difference data, quality control via rough estimates of the propagation speed and attenuation strength, and joint inversion of multiple events using the MCMC algorithm. The proposed method eliminates the need for subjective tuning of data weights and avoids relying on prior knowledge of subsurface structures, local site effects, and source amplitudes. Although some subjective choices are still necessary to set quality control thresholds for  $Q_S$  and  $B$ , these choices do not distort the uncertainty estimation. When applied to real data, the proposed method demonstrated its effectiveness. Appropriately weighting data by their uncertainties was shown to mitigate the undesirable influence of low-quality data (Figs 8c and d), and the correction terms significantly reduced systematic biases (Fig. 8b). Furthermore, using a probabilistic mapping technique allowed us to better comprehend the detailed patterns in locations of tectonic tremors (Fig. 9c). Specifically, we were able to identify striations in the tremor sources. This provides valuable insights into the underlying structural factors that favor tremor activities.

The proposed method still has room for improvement. One of the main assumptions is that the subsurface structures for  $V_S$  and  $Q_S$  are uniform, which can potentially impact the results. Using more sophisticated correction factors, such as source-specific corrections, may help address this bias (e.g., Lomax & Savvaidis, 2022; Richards-Dinger & Shearer, 2000). Alternatively, the spatial variation of  $V_S$  and  $Q_S$  can be solved as unknown parameters, similar to a tomographic approach. The narrow peaks observed in the posterior probabilities (Figs 6e and f) suggest that such an attempt could be promising.

One aspect that we did not discuss in the present study is the criteria for detecting tectonic tremors. In this study, we used the 98th percentile of the histograms of cross-correlation coefficients as a threshold, which was an arbitrary choice. However, the propagation-based quality control in Step 2 of the proposed method provides an alternative approach to detecting tremors. Specifically, applying the selection criteria based on  $V_S$  and  $B$  to all time windows not prescreened by cross-correlation coefficients can incorporate wave-propagation information into the detection process, which would increase its robustness compared to relying solely on waveform similarities. However, one drawback of this wave-propagation-based detection is that it requires high signal-to-noise ratios across the entire seismic network. Solving this problem is left for future work, but using such an objective detection method would help illuminate other important aspects of tectonic tremors, such as the frequency distribution (e.g., Nakano et al., 2019).

While obtaining the detailed features of tremor locations is key to understanding the physical processes behind them, it is particularly challenging for offshore regions, where the accurate location of tremors is hindered by strong heterogeneities in the shallow sedimentary structure. Our results demonstrated that our proposed method is applicable even to such challenging ocean-bottom data. Tectonic tremors that occur in shallow subduction zones remain underexplored. We believe that applying our proposed technique can shed new light on these phenomena.

## **Appendix A. Maximum likelihood estimation for the amplitude ratio**

Consider two waveforms  $u_1(t)$  and  $u_2(t)$  mutually equivalent except for their normalization constants:

$$u_1(t) - A_{12} \cdot u_2(t) = \varepsilon(t), \quad (A1)$$

where  $A_{12}$  is a time-invariant constant representing an amplitude ratio and  $\varepsilon(t)$  is noise contribution. If the noise is assumed to obey a Gaussian distribution (i.e.,  $\varepsilon(t) \sim N(0, \sigma^2)$ ) and to be temporarily independent, the likelihood of the amplitude ratio  $\mathcal{L}(A_{12})$  can be expressed as

$$\mathcal{L}(A_{12}) = \frac{1}{(2\pi\sigma^2)^{\frac{N}{2}}} \prod_{t=1}^N \exp\left(-\frac{(u_1(t) - A_{12} \cdot u_2(t))^2}{2\sigma^2}\right). \quad (A2)$$

Maximizing Equation (A2) corresponds to minimizing the sum of the exponents, which can be achieved under the following condition:

$$\frac{\partial}{\partial A_{12}} \sum_{t=1}^N (u_1(t) - A_{12} \cdot u_2(t))^2 = 0. \quad (A3)$$

The left-hand side of Equation (A3) can be rearranged as follows:

$$\frac{\partial}{\partial A_{12}} \sum_{t=1}^N (u_1(t) - A_{12} \cdot u_2(t))^2 = -2 \left( \sum_{t=1}^N u_1(t)u_2(t) \right) + 2A_{12} \left( \sum_{t=1}^N u_2(t)u_2(t) \right). \quad (A4)$$

From Equations (A3) and (A4), we obtain the MLE of the amplitude ratio:

$$A_{12}^{MLE} = \sum_{t=1}^N u_1(t)u_2(t) / \sum_{t=1}^N u_2(t)u_2(t). \quad (A5)$$

### **Data availability**

Software for the proposed method has been developed on a GitHub repository and will be open by publication. The continuous waveform data from DONET stations are publicly open (National Research Institute for Earth Science and Disaster Resilience, 2019). The continuous waveform data from temporary OBSs are available from the corresponding author upon reasonable request.

### **Acknowledgments**

We thank cruise members of R/V Shinsei-Maru, who played an integral role in acquiring the OBS data. We also thank Shukei Ohyanagi and Atikul Haque Farazi for their assistance during the research cruise and the technical staffs at Earthquake Research Institute, The University of Tokyo, for maintaining OBSs.

### **Author contribution**

Takeshi Akuhara:

Conceptualization, Formal analysis, Funding acquisition, Investigation, Methodology, Project administration, Resources, Software, Visualization, Writing – original draft

Yusuke Yamashita:

Data curation, Investigation, Resources, Writing – review & editing

Hiroko Sugioka:

Data curation, Investigation, Resources, Writing – review & editing

Masanao Shinohara:

Data curation, Funding acquisition, Resources, Writing – review & editing

## References

- Akuhara, T., Tsuji, T., & Tonegawa, T. (2020). Overpressured Underthrust Sediment in the Nankai Trough Forearc Inferred From Transdimensional Inversion of High-Frequency Teleseismic Waveforms. *Geophysical Research Letters*, *47*(15). <https://doi.org/10.1029/2020GL088280>
- Araki, E., Saffer, D. M., Kopf, A. J., Wallace, L. M., Kimura, T., Machida, Y., et al. (2017). Recurring and triggered slow-slip events near the trench at the Nankai Trough subduction megathrust. *Science*, *356*(6343), 1157–1160. <https://doi.org/10.1126/science.aan3120>
- Brown, K. M., Tryon, M. D., DeShon, H. R., Dorman, L. R. M., & Schwartz, S. Y. (2005). Correlated transient fluid pulsing and seismic tremor in the Costa Rica subduction zone. *Earth and Planetary Science Letters*, *238*(1–2), 189–203. <https://doi.org/10.1016/j.epsl.2005.06.055>
- Cruz-Atienza, V. M., Villafuerte, C., & Bhat, H. S. (2018). Rapid tremor migration and pore-pressure waves in subduction zones. *Nature Communications*, *9*(1). <https://doi.org/10.1038/s41467-018-05150-3>
- Geyer, C. J. (1991). Markov Chain Monte Carlo Maximum Likelihood. *Computing Science and Statistics: Proceedings of the 23rd Symposium on the Interface*, (1), 156–163.
- Ghosh, A., Vidale, J. E., Sweet, J. R., Creager, K. C., Wech, A. G., Houston, H., & Brodsky, E. E. (2010). Rapid, continuous streaking of tremor in Cascadia. *Geochemistry, Geophysics, Geosystems*, *11*(12), 1–10. <https://doi.org/10.1029/2010GC003305>
- Hashimoto, Y., Sato, S., Kimura, G., Kinoshita, M., Miyakawa, A., Moore, G. F., et al. (2022). Décollement geometry controls on shallow very low frequency earthquakes. *Scientific Reports*, *12*(1), 2677. <https://doi.org/10.1038/s41598-022-06645-2>
- Houston, H., Delbridge, B. G., Wech, A. G., & Creager, K. C. (2011). Rapid tremor reversals in Cascadia generated by a weakened plate interface. *Nature Geoscience*, *4*(6), 404–409. <https://doi.org/10.1038/ngeo1157>
- Husker, A. L., Kostoglodov, V., Cruz-Atienza, V. M., Legrand, D., Shapiro, N. M.,

- Payero, J. S., et al. (2012). Temporal variations of non-volcanic tremor (NVT) locations in the Mexican subduction zone: Finding the NVT sweet spot. *Geochemistry, Geophysics, Geosystems*, 13(3).  
<https://doi.org/10.1029/2011GC003916>
- Ide, S. (2010). Striations, duration, migration and tidal response in deep tremor. *Nature*, 466(7304), 356–359. <https://doi.org/10.1038/nature09251>
- Ide, S., Beroza, G. C., Shelly, D. R., & Uchide, T. (2007). A scaling law for slow earthquakes. *Nature*, 447(7140), 76–79. <https://doi.org/10.1038/nature05780>
- Kaneda, Y., Kawaguchi, K., Araki, E., Matsumoto, H., Nakamura, T., Kamiya, S., et al. (2015). Development and application of an advanced ocean floor network system for megathrust earthquakes and tsunamis. In *SEAFLOOR OBSERVATORIES* (pp. 643–662). Berlin, Heidelberg: Springer Berlin Heidelberg.  
[https://doi.org/10.1007/978-3-642-11374-1\\_25](https://doi.org/10.1007/978-3-642-11374-1_25)
- Kawaguchi, K., Kaneko, S., Nishida, T., & Komine, T. (2015). Construction of the DONET real-time seafloor observatory for earthquakes and tsunami monitoring. In *SEAFLOOR OBSERVATORIES* (pp. 211–228). Berlin, Heidelberg: Springer Berlin Heidelberg. [https://doi.org/10.1007/978-3-642-11374-1\\_10](https://doi.org/10.1007/978-3-642-11374-1_10)
- Li, K. L., Bean, C. J., Bell, A. F., Ruiz, M., Hernandez, S., & Grannell, J. (2022). Seismic tremor reveals slow fracture propagation prior to the 2018 eruption at Sierra Negra volcano, Galápagos. *Earth and Planetary Science Letters*, 586, 117533. <https://doi.org/10.1016/j.epsl.2022.117533>
- Lomax, A., & Savvaidis, A. (2022). High-Precision Earthquake Location Using Source-Specific Station Terms and Inter-Event Waveform Similarity. *Journal of Geophysical Research: Solid Earth*, 127(1). <https://doi.org/10.1029/2021JB023190>
- Maeda, T., & Obara, K. (2009). Spatiotemporal distribution of seismic energy radiation from low-frequency tremor in western Shikoku, Japan. *Journal of Geophysical Research: Solid Earth*, 114(10), 1–17. <https://doi.org/10.1029/2008JB006043>
- Mizuno, N., & Ide, S. (2019). Development of a modified envelope correlation method based on maximum - likelihood method and application to detecting and locating deep tectonic tremors in western Japan. *Earth, Planets and Space*.  
<https://doi.org/10.1186/s40623-019-1022-x>
- Nakano, M., Yabe, S., Sugioka, H., Shinohara, M., & Ide, S. (2019). Event Size Distribution of Shallow Tectonic Tremor in the Nankai Trough. *Geophysical Research Letters*, 46(11), 5828–5836. <https://doi.org/10.1029/2019GL083029>
- Nishikawa, T., Matsuzawa, T., Ohta, K., Uchida, N., Nishimura, T., & Ide, S. (2019). The slow earthquake spectrum in the Japan Trench illuminated by the S-net

- seafloor observatories. *Science*, 365(6455), 808–813.  
<https://doi.org/10.1126/science.aax5618>
- National Research Institute for Earth Science and Disaster Resilience (2019). NIED DONET, National Research Institute for Earth Science and Disaster Resilience, <https://doi.org/10.17598/nied.0008>
- Obara, K. (2002). Nonvolcanic Deep Tremor Associated with Subduction in Southwest Japan. *Science*, 296(5573), 1679–1681. <https://doi.org/10.1126/science.1070378>
- Obara, K., & Kato, A. (2016). Connecting slowearthquakes to huge earthquakes. *Science*, 353(6296), 253–257. <https://doi.org/10.1126/science.aaf1512>
- Ogiso, M., & Tamaribuchi, K. (2022). Spatiotemporal evolution of tremor activity near the Nankai Trough trench axis inferred from the spatial distribution of seismic amplitudes. *Earth, Planets and Space*. <https://doi.org/10.1186/s40623-022-01601-w>
- Payero, J. S., Kostoglodov, V., Shapiro, N., Mikumo, T., Iglesias, A., Pérez-Campos, X., & Clayton, R. W. (2008). Nonvolcanic tremor observed in the Mexican subduction zone. *Geophysical Research Letters*, 35(7), 1–6.  
<https://doi.org/10.1029/2007GL032877>
- Plata-Martinez, R., Ide, S., Shinohara, M., Garcia, E. S., Mizuno, N., Dominguez, L. A., et al. (2021). Shallow slow earthquakes to decipher future catastrophic earthquakes in the Guerrero seismic gap. *Nature Communications*, 12(1).  
<https://doi.org/10.1038/s41467-021-24210-9>
- Richards-Dinger, K. B., & Shearer, P. M. (2000). Earthquake locations in southern California obtained using source-specific station terms. *Journal of Geophysical Research*, 105(B5), 10939. <https://doi.org/10.1029/2000JB900014>
- Rogers, G. (2003). Episodic Tremor and Slip on the Cascadia Subduction Zone: The Chatter of Silent Slip. *Science*, 300(5627), 1942–1943.  
<https://doi.org/10.1126/science.1084783>
- Rubin, A. M. (2011). Designer friction laws for bimodal slow slip propagation speeds. *Geochemistry, Geophysics, Geosystems*, 12(4), 1–22.  
<https://doi.org/10.1029/2010GC003386>
- Sambridge, M. (2014). A Parallel Tempering algorithm for probabilistic sampling and multimodal optimization. *Geophysical Journal International*, 196(1), 357–374.  
<https://doi.org/10.1093/gji/ggt342>
- Takemura, S., Yabe, S., & Emoto, K. (2020). Modelling high-frequency seismograms at ocean bottom seismometers: Effects of heterogeneous structures on source parameter estimation for small offshore earthquakes and shallow low-frequency

- tremors. *Geophysical Journal International*, 223(3), 1708–1723.  
<https://doi.org/10.1093/gji/ggaa404>
- Takemura, S., Obara, K., Shiomi, K., & Baba, S. (2022). Spatiotemporal Variations of Shallow Very Low Frequency Earthquake Activity Southeast Off the Kii Peninsula, Along the Nankai Trough, Japan. *Journal of Geophysical Research: Solid Earth*, 127(3). <https://doi.org/10.1029/2021JB023073>
- Todd, E. K., Schwartz, S. Y., Mochizuki, K., Wallace, L. M., Sheehan, A. F., Webb, S. C., et al. (2018). Earthquakes and Tremor Linked to Seamount Subduction During Shallow Slow Slip at the Hikurangi Margin, New Zealand. *Journal of Geophysical Research: Solid Earth*, 123(8), 6769–6783. <https://doi.org/10.1029/2018JB016136>
- Tsuji, T., Dvorkin, J., Mavko, G., Nakata, N., Matsuoka, T., Nakanishi, A., et al. (2011). V P / V S ratio and shear-wave splitting in the Nankai Trough seismogenic zone: Insights into effective stress, pore pressure, and sediment consolidation. *Geophysics*, 76(3), WA71–WA82. <https://doi.org/10.1190/1.3560018>
- VanDecar, J. C., & Crosson, R. S. (1990). Determination of teleseismic relative phase arrival times using multi-channel cross-correlation and least squares. *Bulletin of the Seismological Society of America*, 80(1), 150–169. Retrieved from <http://www.bssaonline.org/content/80/1/150.short>
- Yabe, S., Baba, S., Tonegawa, T., Nakano, M., & Takemura, S. (2021). Seismic energy radiation and along-strike heterogeneities of shallow tectonic tremors at the Nankai Trough and Japan Trench. *Tectonophysics*, 800, 228714.  
<https://doi.org/10.1016/j.tecto.2020.228714>
- Yamashita, Y., Yakiwara, H., Asano, Y., Shimizu, H., Uchida, K., Hirano, S., et al. (2015). Migrating tremor off southern Kyushu as evidence for slow slip of a shallow subduction interface. *Science*, 348(6235), 676–679.  
<https://doi.org/10.1126/science.aaa4242>



*Supplementary Material*

**Locating tectonic tremors with uncertainty estimates: Time- and amplitude-difference optimization, wave propagation-based quality control, and Bayesian inversion**

Takeshi Akuhara<sup>1</sup>, Yusuke Yamashita<sup>2</sup>, Hiroko Sugioka<sup>3</sup>, Masanao Shinohara<sup>1</sup>

<sup>1</sup>Earthquake Research Institute, The University of Tokyo

<sup>2</sup>Disaster Prevision Research Institute, Kyoto University

<sup>3</sup>Department of Planetology, Graduate School of Science, Kobe University

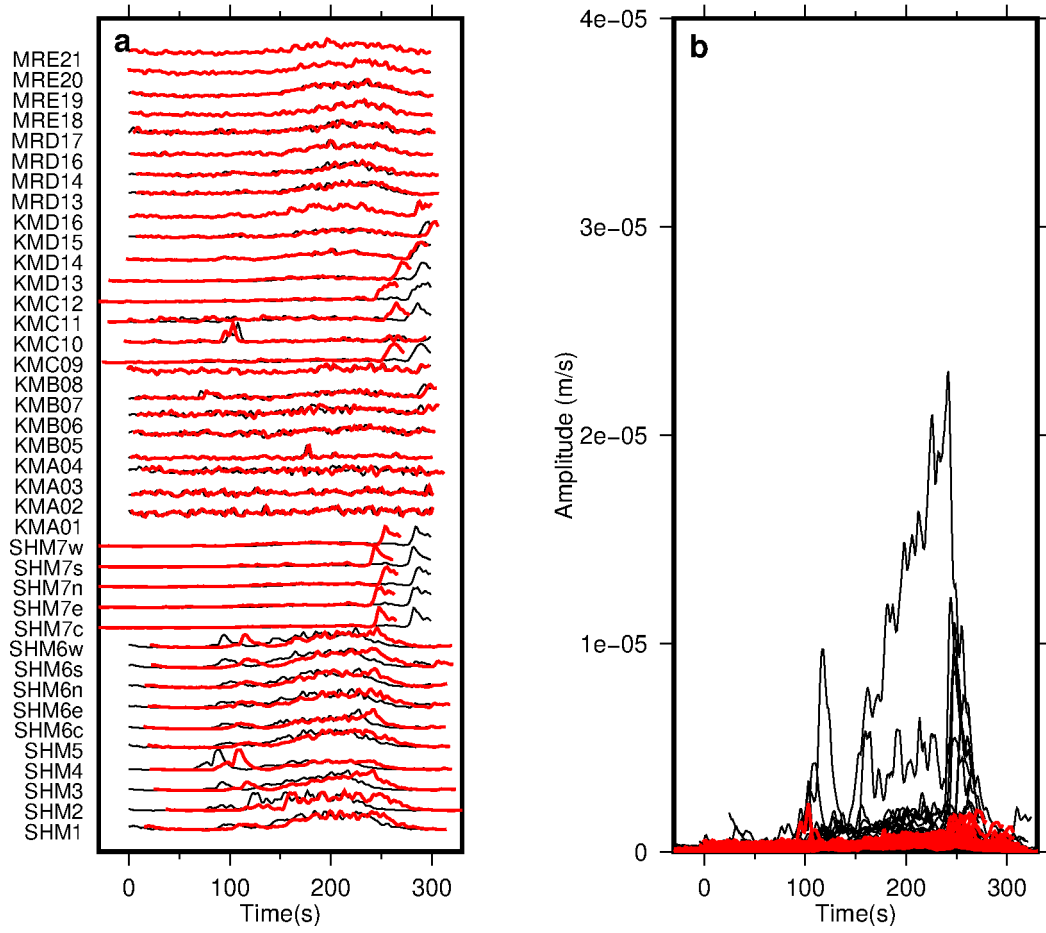


**Figure S1.** A failure case of the optimization step. Notations are the same as Fig. 2.

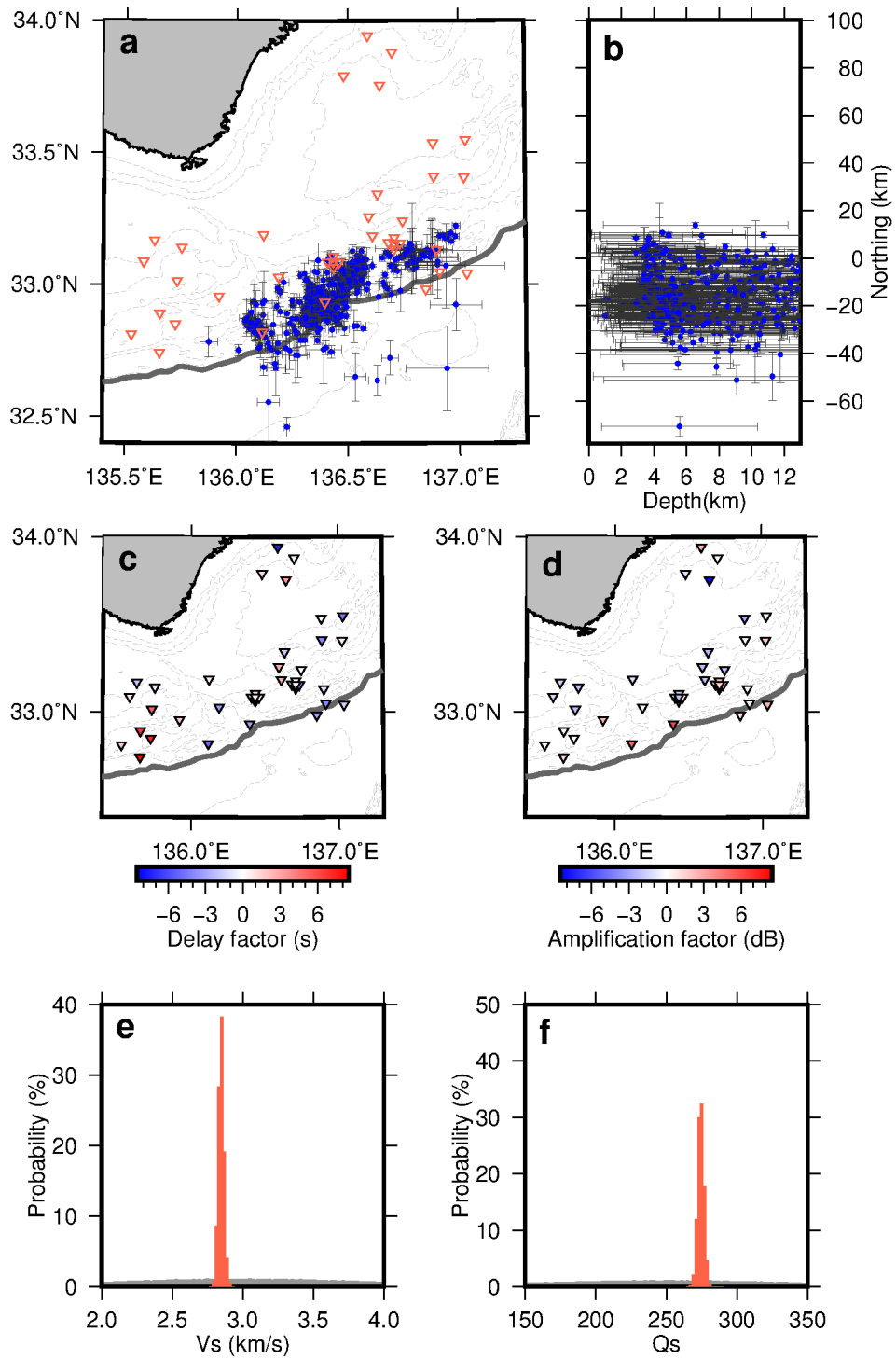


**Figure S2.** Inversion results without tempering. Notations are the same as Fig. 6.

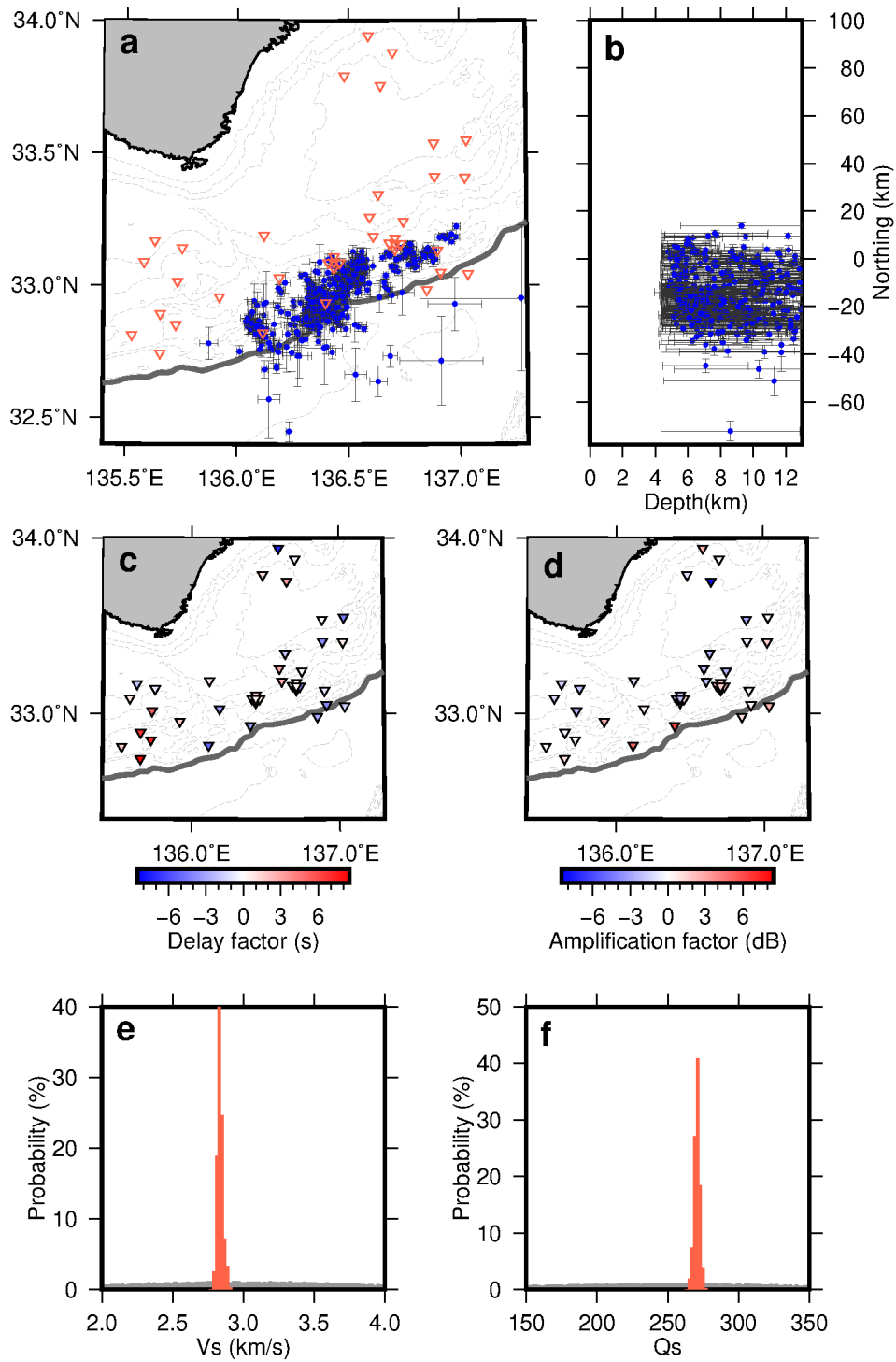


**Figure S3.** Inversion results where  $z_0$  is set to 4.5 km for the depth prior (see Eq. 19). Notations are the same as Fig. 6.